

Article

One-Step Synthesis of Ultrathin High-Entropy Layered Double Hydroxides for Ampere-Level Water Oxidation

Jianlei Jing, Wei Liu *, Tianshui Li, Xiaoqian Ding, Wenhai Xu, Mengze Ma, Daojin Zhou, Yaping Li * and Xiaoming Sun

State Key Laboratory of Chemical Resource Engineering, College of Chemistry, University of Chemical Technology, Beijing 100029, China; 2021200874@mail.buct.edu.cn (J.J.); 2021400265@buct.edu.cn (T.L.); 2021210570@buct.edu.cn (X.D.); 2021210642@buct.edu.cn (W.X.); 2022200974@buct.edu.cn (M.M.); zhoujd@buct.edu.cn (D.Z.); sunxm@mail.buct.edu.cn (X.S.)

* Correspondence: 2022400260@buct.edu.cn (W.L.); liyp@mail.buct.edu.cn (Y.L.)

Abstract: The development of high-entropy anodes, known for their excellent catalytic activity for water oxidation, can depress the energy consumption of hydrogen production by water electrolysis. However, the complex preparation methods and poor stability hindered their practical application. In this work, a one-step co-precipitation method has been modified to rapidly synthesize ultrathin high-entropy layered double hydroxide containing Ni, Co, Fe, Cr, Zn. Through the rational selection of metal elements, the stability of the optimized anode under Ampere-level current density has been significantly improved. Compared to NiFe-LDH, the active site leaching of high-entropy LDH is reduced by 42.7%, and as a result, it achieves a performance decay that is approximately eight times lower than that of NiFe-LDH. Experiment results show that the active sites in the high-entropy LDH can maintain a relatively low oxidation state both before and after activation, thus preventing material deactivation caused by excessive oxidation.

Keywords: high entropy; layered double hydroxides; oxygen evolution reaction



Citation: Jing, J.; Liu, W.; Li, T.; Ding, X.; Xu, W.; Ma, M.; Zhou, D.; Li, Y.; Sun, X. One-Step Synthesis of Ultrathin High-Entropy Layered Double Hydroxides for Ampere-Level Water Oxidation. *Catalysts* **2024**, *14*, 171. <https://doi.org/10.3390/catal14030171>

Academic Editor: Nicolas Alonso-Vante

Received: 4 February 2024

Revised: 23 February 2024

Accepted: 23 February 2024

Published: 27 February 2024



Copyright: © 2024 by the authors. Licensee MDPI, Basel, Switzerland. This article is an open access article distributed under the terms and conditions of the Creative Commons Attribution (CC BY) license (<https://creativecommons.org/licenses/by/4.0/>).

1. Introduction

Hydrogen production through water splitting is recognized as an effective solution to the global energy crisis [1]. However, the sluggish kinetics of the oxygen evolution reaction (OER) at the anode side result in increased energy consumption, posing a significant obstacle to its widespread implementation [2–5]. Therefore, the search for electrocatalysts with excellent OER performance to meet the needs of the future is one of the fundamental driving forces in the materials science community [6–8].

Layered double hydroxide (LDH) is a typical two-dimensional layered structure consisting of positively charged octahedral hydroxide layers, interlayer anions and interlayer water [9–11]. The adjustable metal cations and exchangeable interlayer anions deliver flexibility to LDHs catalysts, which are considered as catalysts with great application prospects. In various previous studies, it was found that using different exfoliation strategies to achieve the ultrathin layer or even single-layer structure of LDH could expose more active sites and thus enhance the activity [12–14]. In addition, the exploration of ternary, quaternary or even high-entropy polymetallic LDH also provides another optimization strategy [15,16]. With the adjustment of and increase in metal ion types, polymetallic LDH outperforms traditional binary LDH. High-entropy material uses the high configurational entropy of the structure itself to stabilize the lattice structure of the material, and can stabilize the Gibbs free energy of the system, being more structurally stable to low-entropy materials [17–19]. In recent years, it has been found that high-entropy materials have slow diffusion, lattice distortion, cocktail effect and so on [20]. Studies on high-entropy material (HEM) have been carried out on high-entropy oxides [21–23], high-entropy nitrides [24],

high-entropy carbides and other materials [25]. With this in mind, combining the particularity of the high-entropy structure with the adjustability of LDH, it will be possible to obtain a fascinating new type of water oxidation electrocatalyst.

In this work, ultrathin high-entropy layered double hydroxides containing Ni, Co, Fe, Zn, Cr (U-NiFeZnCoCr-LDH) were prepared by a modified co-precipitation method. By introducing formamide (FA) during synthesis, the thickness was controlled at approximately 2 nm. Through the rational selection of metal elements, the dual-improvement of activity and stability was achieved in U-NiFeZnCoCr-LDH, which operates stably for 180 h at 800 mA cm⁻². ICP-MS results show that the dissolution of active sites during stability testing is reduced by 42.7% compared to NiFe-LDH, demonstrating the industrialization potential of this material.

2. Results

The synthesis of ultrathin layered double hydroxides (LDH) can be achieved through bottom-up and top-down methods. The bottom-up approach typically entails the preparation of multilayer LDH followed by the separation of the layers using exfoliation techniques. This method involves multiple steps and is associated with high costs for the exfoliation step. In contrast, the top-down method involves the control of conditions for the nucleation and growth of LDH to spontaneously form ultrathin structures. Therefore, although the top-down method has lower cost, it is usually more complex.

In this work, the ultrathin high-entropy NiFeZnCoCr-LDH was synthesized using a facile bottom-up method (Figure 1a). The synthesis method represents a modification of the co-precipitation technique. Solution A comprises multiple M(NO₃)_n species (M=Ni, Fe, Zn, Co, Cr), whereas solution B consists of a 1 M NaOH solution. In the conventional co-precipitation method, solution C typically consists of an aqueous solution of sodium carbonate. This facilitates the incorporation of carbonate ions into the interlayers of LDH during its nucleation and growth, resulting in the formation of a more stable structure. But in this modified synthesis method, the sodium carbonate in solution C is replaced with sodium nitrate, enabling the insertion of nitrate ions. Moreover, formamide (FA) was employed in solution C to facilitate the spontaneous exfoliation of LDH while it was growing [11–13].

By controlling the presence or absence of FA in solution C, NiFeZnCoCr-LDH and U-NiFeZnCoCr-LDH can be synthesized, respectively. The X-ray diffraction patterns (XRD, Figure 1b) of both samples exhibit similar diffraction peaks to those of NiFe-LDH (JCPDS #40-0215), with signals at 11.4 and 23.0° attributed to the (003) and (006) planes, respectively, which result from the layered stacking of monolayer LDH. Due to the reduced thickness of U-NiFeZnCoCr-LDH along the *c* axial direction, the intensity of the aforementioned diffraction peaks is significantly weaker than that of NiFeZnCoCr-LDH. Additionally, the signals attributed to the (012) and (110) planes, corresponding to the in-plane facets, demonstrate no significant changes, indicating that the decreased intensity of (003) and (006) is not a result of reduced crystallinity in U-NiFeZnCoCr-LDH. High-resolution transmission electron microscopy (HRTEM) images reveal lattice fringes with a width of 0.27 nm, corresponding to the (101) plane, further confirming the successful synthesis of U-NiFeZnCoCr-LDH and bolstering the conclusions drawn from XRD. Atomic force microscopy (AFM) was used to measure the dimensions of U-NiFeZnCoCr-LDH, as depicted in Figure 1d. Individual nanosheets exhibit a width of approximately 100 nm and a thickness of only about 2 nm. This finding suggests that U-NiFeZnCoCr-LDH is highly dispersed following exfoliation, leading to a substantial increase in specific surface area and promoting the exposure of highly active sites during electrocatalytic OER.

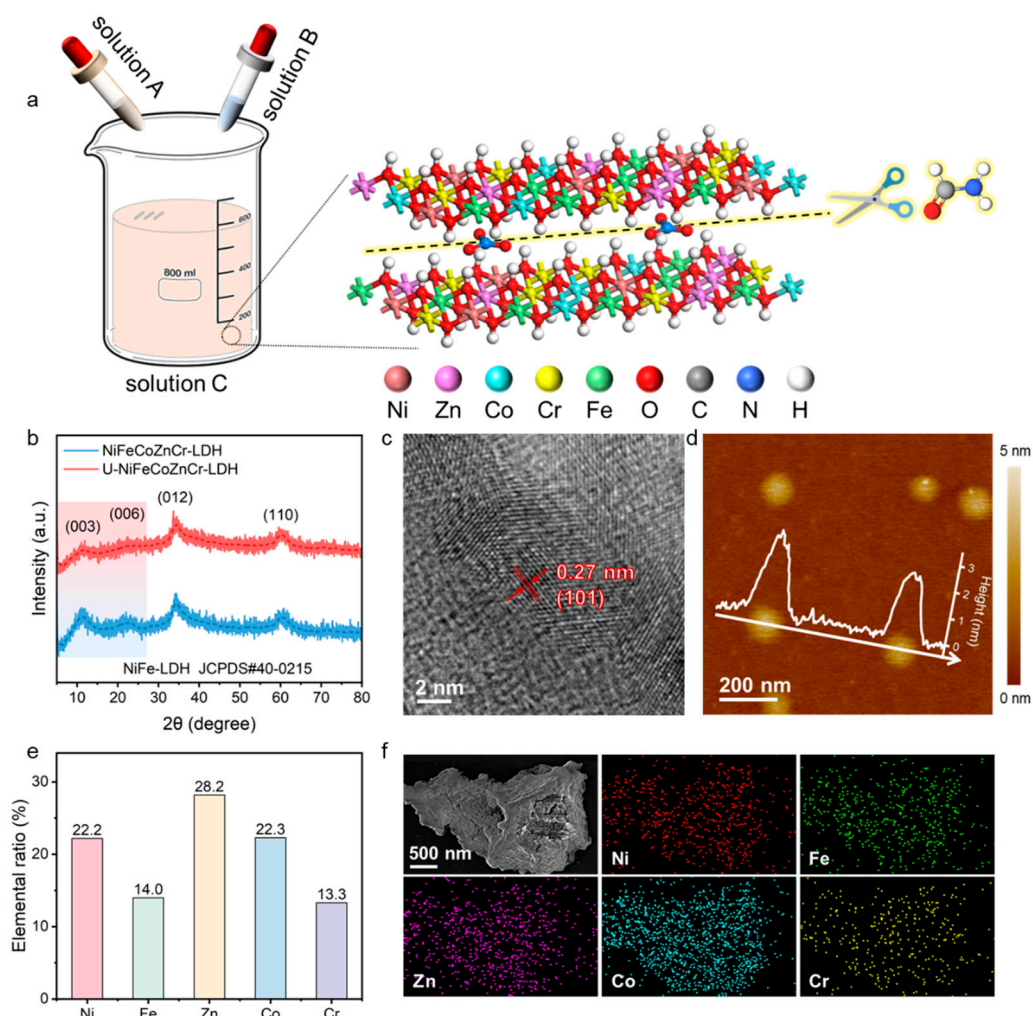


Figure 1. (a) Synthetic scheme of U-NiFeZnCoCr-LDH, (b) XRD patterns of NiFeZnCoCr-LDH and U-NiFeZnCoCr-LDH, (c) HRTEM image, (d) AFM image, (e) The atomic ratio, (f) SEM image and the corresponding EDS elemental mapping of U-NiFeZnCoCr-LDH.

The proportion of various metal elements in U-NiFeZnCoCr-LDH was verified by energy-dispersive X-ray spectroscopy (EDS, Figure 1e). The results indicate that Ni, Fe, Zn, Co and Cr account for 22.2%, 14.0%, 28.2%, 22.3% and 13.3% (atomic ratio), respectively. Among them, Ni, Zn and Co are divalent metal elements (M^{2+}), while Fe and Cr are trivalent metal elements (M^{3+}). Therefore, the ratio of M^{2+}/M^{3+} in the material can be calculated to be approximately 73/27. This result is consistent with the M^{2+}/M^{3+} ratio previously mentioned in the XRD analysis with JCPDS #40-0215 ($Ni_{0.75}Fe_{0.25}(CO_3)_{0.125}(OH)_2 \cdot 0.38H_2O$). Furthermore, EDS elemental mapping in Figure 1f further confirms that the metal elements are uniformly dispersed without phase separation.

To illustrate the versatility of this synthesis method, ultrathin NiFeZnCoAl-LDH and NiFeZnCoMn-LDH were synthesized using the same approach. XRD patterns in Figure S1 also revealed weak signals for (003) and (006). Furthermore, as shown in Figure S2, EDS-mapping results further demonstrated the uniform distribution of various metal elements. These findings confirm the successful synthesis of U-NiFeZnCoAl-LDH and U-NiFeZnCoMn-LDH, indicating the scalability of this modified co-precipitation method.

Fourier transform infrared spectroscopy (FTIR) was utilized to gather additional information about the surface coordination environment. As shown in Figure 2a, both NiFeZnCoCr-LDH and U-NiFeZnCoCr-LDH exhibit similar N-O stretching vibrations at 1384 cm^{-1} , indicating the introduction of nitrate intercalation during synthesis [26]. However, U-NiFeZnCoCr-LDH displays a distinctive C=O stretching vibration peak at

1692 cm^{-1} , attributed to the amide group of FA [27]. The existence of this vibration signal suggests that the introduced formamide partially replaced NO_3^- and penetrated the interlayer, resulting in the LDH exfoliation and formation of the ultrathin LDH structure.

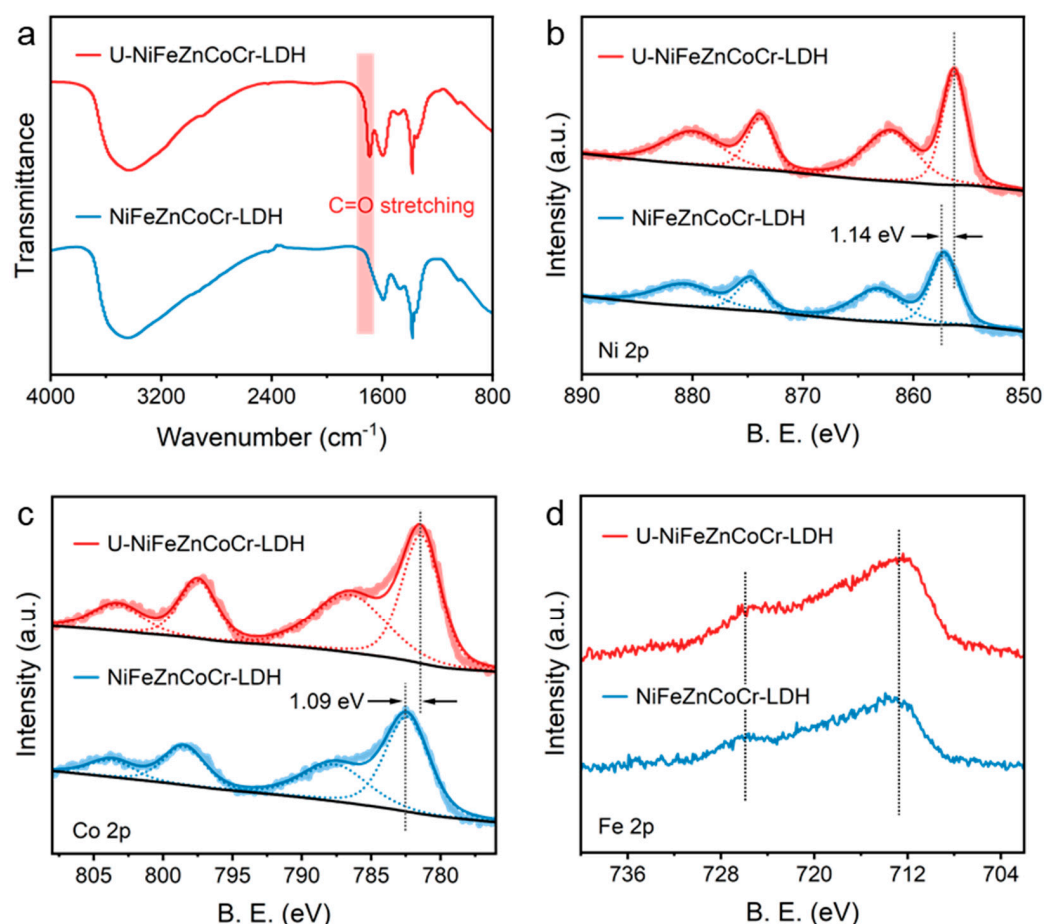


Figure 2. (a) FTIR spectra, and high-resolution XPS spectra of (b) Ni 2p, (c) Co 2p and (d) Fe 2p of NiFeZnCoCr-LDH and U-NiFeZnCoCr-LDH.

The addition of FA not only induces changes in material thickness but also brings about alterations in the electron density around the metal elements due to its inherent reducibility. As illustrated in the high-resolution X-ray photoelectron spectroscopy (XPS) spectra of the Ni 2p orbitals (Figure 2b), the signals attributed to $\text{Ni}^{2+} 2p_{3/2}$ (approximately 857 eV) and $\text{Ni}^{2+} 2p_{1/2}$ (approximately 874 eV) in U-NiFeZnCoCr-LDH [28] demonstrate a notable shift toward lower binding energy (B.E.) compared to NiFeZnCoCr-LDH, by approximately 1.14 eV. Likewise, the Co 2p (Figure 2c) and Zn 2p (Figure S3) signals also exhibit negative shifts by 1.09 eV and 1.03 eV, respectively [29]. This outcome indicates that M^{2+} is susceptible to the reducing environment created by FA, resulting in an increase in the electron density around it and maintaining a lower oxidation state. In contrast, the high-resolution XPS spectra of Fe 2p (Figure 2d) and Cr 2p (Figure S4) show a very slight trend of signal shift toward lower B.E., suggesting that M^{3+} is almost unaffected by FA [30,31]. It is widely recognized that the active sites of NiFe-LDH are prone to being excessively oxidized and dissolved during the OER process, contributing to the poor stability of NiFe-LDH. The introduction of FA induces an electron rearrangement, which is anticipated to maintain the active sites of the electrocatalyst at lower oxidation states during OER, thereby enhancing stability.

The OER performance of U-NiFeZnCoCr-LDH was evaluated in an alkaline electrolyte (1 M KOH) using a conventional three-electrode system. The polarization curves in Figure 3a illustrate that U-NiFeZnCoCr-LDH exhibits outstanding activity, achieving a cur-

rent density of 10 mA cm^{-2} with an overpotential of only 268 mV. In contrast, NiFeZnCoCr-LDH and NiFe-LDH require overpotentials of 310 mV and 337 mV, respectively. Additionally, the polarization curve of bare nickel foam is depicted in Figure S5a, with its associated redox peaks, illustrated in Figure S5b, to determine the background current. The redox peaks corresponding to $\text{Ni}^{2+}/\text{Ni}^{3+}$ were detected from 1.1–1.6 V vs. RHE. Notably, no redox peaks for $\text{Ni}^0/\text{Ni}^{2+}$ were observed within the tested voltage range due to their occurrence typically around -0.257 V vs. RHE.

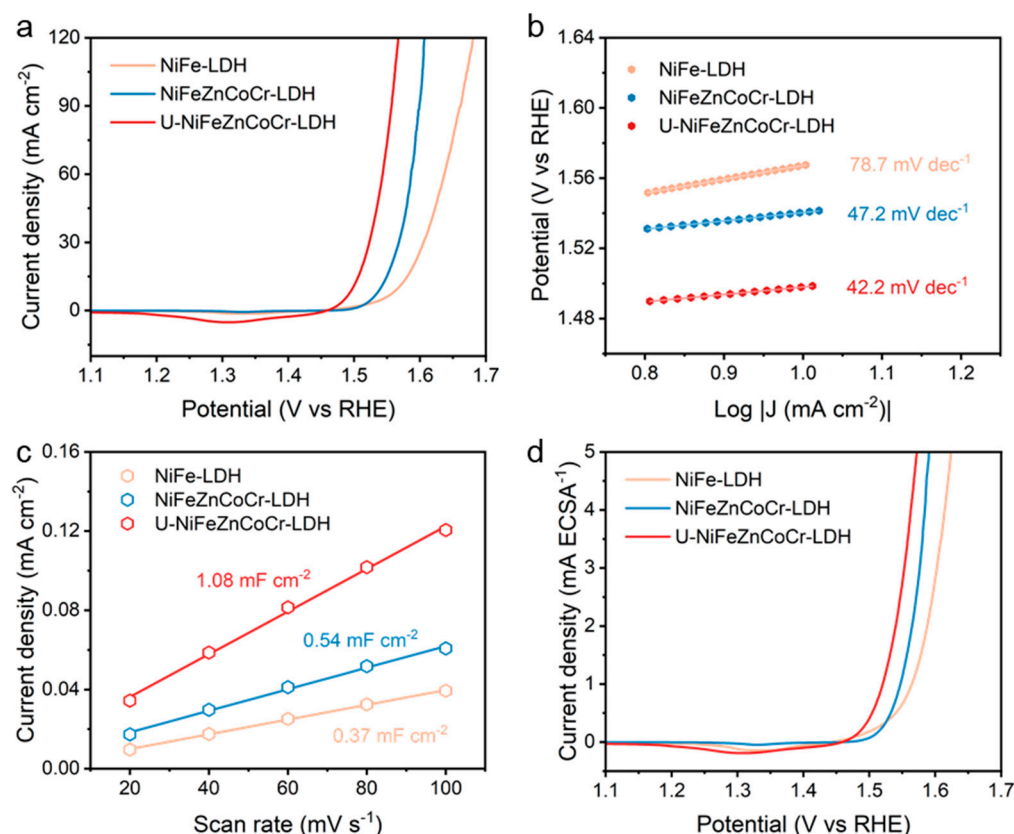


Figure 3. (a) Polarization curves, (b) Tafel slope of NiFe-LDH, NiFeZnCoCr-LDH and U-NiFeZnCoCr-LDH, (c) The extraction of the C_{dl} for the estimation of the ECSA, and (d) the ECSA-normalized polarization curves NiFe-LDH, NiFeZnCoCr-LDH and U-NiFeZnCoCr-LDH.

As depicted in Figure 3b, U-NiFeZnCoCr-LDH (42.2 mV dec^{-1}) and NiFeZnCoCr-LDH (47.2 mV dec^{-1}) display similar Tafel slopes, both significantly lower than that of NiFe-LDH (78.7 mV dec^{-1}). This suggests that these two high-entropy LDHs exhibit superior OER reaction kinetics compared to low-entropy LDHs. The enhanced electrocatalytic activity can be attributed to their intrinsic high configurational disorder, which facilitates favorable interactions between the active sites and reaction intermediates [32,33].

Subsequently, the double-layer capacitance (C_{dl} , as shown in Figures 3c and S6) was utilized to determine the electrochemically active surface area (ECSA) of these three samples. Notably, U-NiFeZnCoCr-LDH exhibited the highest C_{dl} (1.08 mF cm^{-2}), nearly double that of NiFeZnCoCr-LDH (0.54 mF cm^{-2}). This observation elucidates the similar Tafel slopes of these two high-entropy LDHs, despite significant differences in overpotential. In contrast, NiFe-LDH displayed a much lower C_{dl} (only 0.37 mF cm^{-2}) compared to U-NiFeZnCoCr-LDH. When combined with its unfavorable reaction kinetics reflected by the Tafel slope, this phenomenon further accounts for its lower activity.

After normalizing the current density in Figure 3a to the ECSA of these samples, Figure 3d illustrates that both U-NiFeZnCoCr-LDH and NiFeZnCoCr-LDH exhibit superior activity per unit ECSA compared to NiFe-LDH. While the performance gap between these two high-entropy LDHs is narrowed, U-NiFeZnCoCr-LDH is still advantageous. This

suggests that the addition of FA during the synthesis of U-NiFeZnCoCr-LDH impacts the electron density around the active sites, resulting in better electrocatalytic activity. Furthermore, the ultrathin nature of U-NiFeZnCoCr-LDH enables its electrocatalytic active sites to be fully exposed, further enhancing the OER performance [34,35].

In order to further demonstrate the benefits of the ultrathin characteristics, the OER performance of the aforementioned U-NiFeZnCoAl-LDH and U-NiFeZnCoMn-LDH was also evaluated. As depicted in Figure S7, all of the ultrathin LDHs exhibited lower overpotentials, and the Tafel slopes indicated faster OER kinetics. It is worth noting that U-NiFeZnCoCr-LDH also exhibits significant performance advantages among these samples, showing a lower onset potential and a lower Tafel slope. This indicates that the combination of metal elements used in U-NiFeZnCoCr-LDH is reasonable.

The long-term durability of catalysts is another critical aspect beyond activity, thus the electrocatalytic stability of U-NiFeZnCoCr-LDH and NiFe-LDH was assessed using a two-electrode system, with the current density set above the industrial demand of 800 mA cm^{-2} . The chronopotentiometry curve (Figure 4a) reveals that the system with U-NiFeZnCoCr-LDH as the anode demonstrates no voltage increase over a 180 h test period, whereas the system with NiFe-LDH as the anode experiences a voltage increase of 359 mV. As depicted in Figure 4b, the concentration of Ni ions in the electrolyte after the operation of the two systems was measured using inductively coupled plasma-mass spectrometry (ICP-MS). The results confirmed that NiFe-LDH dissolves a larger amount of Ni^{2+} (approximately 30 ppm), while the dissolution in U-NiFeZnCoCr-LDH is only half of that. Numerous studies have highlighted the significance of Ni-sites in NiFe-based OER electrocatalysts, with their substantial dissolution being considered a contributing factor to electrode performance degradation. The lower dissolution rate of Ni^{2+} in U-NiFeZnCoCr-LDH results in a lower performance decay ratio (-4.8% , representing a 4.8% improvement), while this parameter reaches 8.0% (representing an 8.0% decay) in the NiFe-LDH system.

To elucidate the reason behind the superior electrocatalytic stability of U-NiFeZnCoCr-LDH (even showing improved activity after stability testing), the as-prepared electrode was operated at 100 mA cm^{-2} for 5 h to achieve full activation. As shown in Figure 4c,d, following activation, the signals corresponding to Zn 2p and Cr 2p in U-NiFeZnCoCr-LDH noticeably weakened, while significant K 2s and K 2p signals emerged. This phenomenon arises from Zn and Cr, as amphoteric metal ions tend to dissolve in alkaline electrolytes [36,37]. The substantial attack of OH^- on the electrode surface during electrocatalytic OER further promotes this dissolution process. The dissolution of Zn^{2+} and Cr^{3+} results in the creation of M^{2+} and M^{3+} vacancies, respectively, leading to a more comprehensive exposure of the active sites [38–40]. This enhanced exposure is responsible for the improved OER activity of U-NiFeZnCoCr-LDH during stability testing. Furthermore, as positively charged sites are lost during this process, the electrode adsorbs cations from the electrolyte (primarily K^+) to maintain charge balance, as evidenced by the significant K^+ signal observed in Figure 3c. It is important to note that the F 1s signal originates from the Nafion ionomer added to the catalyst ink and is unrelated to the other observed phenomena. Furthermore, the oxidation states of Co and Ni exhibit minimal changes after activation, with their B.E. even lower than those observed for NiFeZnCoCr-LDH in Figure 2b,c. This finding confirms that during activation, U-NiFeZnCoCr-LDH effectively preserves its active sites in an electron-rich state, thereby substantially reducing their dissolution, as supported by the results presented in Figure 4b.

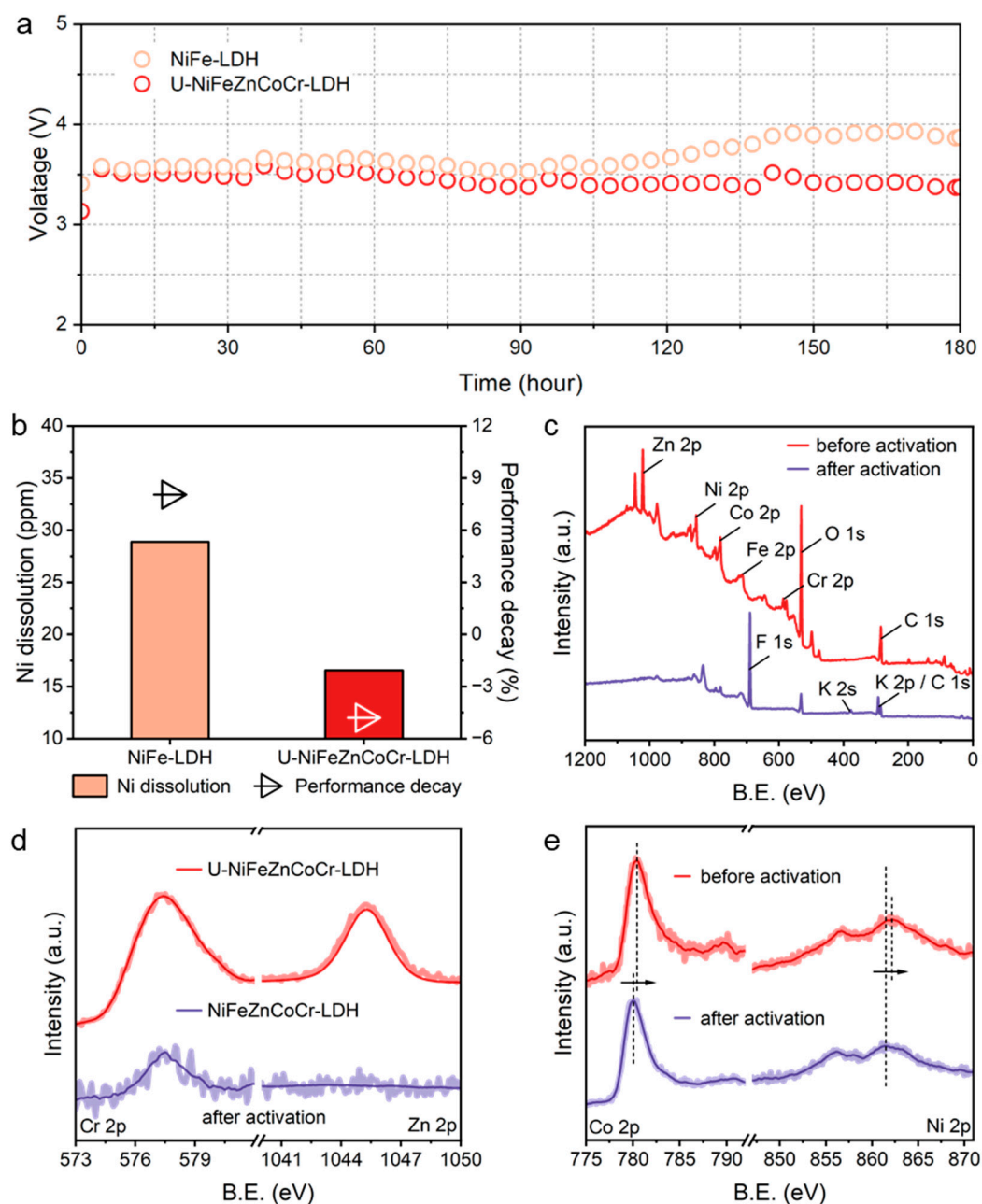


Figure 4. (a) Chronopotentiometry curves at 800 mA cm⁻², (b) the dissolved amount of Ni (left axis) and performance decay ratio (right axis) of NiFe-LDH and U-NiFeZnCoCr-LDH. (c) XPS survey of U-NiFeZnCoCr-LDH before and after activation. High-resolution XPS spectra of (d) Cr 2p, Zn 2p and (e) Co 2p, Ni 2p of U-NiFeZnCoCr-LDH and NiFeZnCoCr-LDH after activation.

3. Material and Methods

3.1. Chemicals

Fe(NO₃)₃·9H₂O, Ni(NO₃)₂·6H₂O, Co(NO₃)₂·6H₂O, ZnCl₂, Cr(NO₃)₃·9H₂O and NaNO₃ were purchased from Aladdin Industrial Corporation. NaOH, KOH and ethanol were purchased from Beijing Chemical Reagents Company (Beijing, China). All the solutions in this work were prepared by deionized water (DI water) with a resistivity ≥ 18 MΩ. And all the chemicals were used as received without further purification.

3.2. Synthesis of U-NiFeZnCoCr-LDH

The preparation of U-NiFeZnCoCr-LDH followed a modified co-precipitation method. In a typical synthesis, 0.2 M $\text{Ni}(\text{NO}_3)_2 \cdot 6\text{H}_2\text{O}$, 0.1 M $\text{Fe}(\text{NO}_3)_3 \cdot 9\text{H}_2\text{O}$, 0.2 M ZnCl_2 , 0.2 M $\text{Co}(\text{NO}_3)_2 \cdot 6\text{H}_2\text{O}$ and 0.1 M $\text{Cr}(\text{NO}_3)_3 \cdot 9\text{H}_2\text{O}$ were dissolved in 20 mL DI water. This solution was labeled as solution A. 1 M NaOH was dissolved in DI water and labeled as solution B. 2 g NaNO_3 was dissolved in 77 mL DI water, then 23 mL FA was added and the mixture was stirred magnetically to form a homogeneous solution, which was labeled as solution C. After heating solution C to 80 °C, solutions A and B were added dropwise while the pH of solution C was maintained at around 10. After 10 min, the product was collected by centrifugation, washed with DI water and ethanol several times, and dried in freeze dryer for 24 h. Nitrogen gas was bubbled into solution C throughout the entire reaction.

3.3. Synthesis of NiFeZnCoCr-LDH

In a typical synthesis, 0.2 M $\text{Ni}(\text{NO}_3)_2 \cdot 6\text{H}_2\text{O}$, 0.1 M $\text{Fe}(\text{NO}_3)_3 \cdot 9\text{H}_2\text{O}$, 0.2 M ZnCl_2 , 0.2 M $\text{Co}(\text{NO}_3)_2 \cdot 6\text{H}_2\text{O}$ and 0.1 M $\text{Cr}(\text{NO}_3)_3 \cdot 9\text{H}_2\text{O}$ were dissolved in 20 mL DI water. This solution was labeled as solution A. 1 M NaOH was dissolved in DI water and labeled as solution B. 2 g NaNO_3 was dissolved in 100 mL DI water, which was labeled as solution C. After heating solution C to 80 °C, solutions A and B were added dropwise while the pH of solution C was maintained at around 10. After 10 min, the product was collected by centrifugation, washed with DI water and ethanol several times, and dried in freeze dryer for 24 h. Nitrogen gas was bubbled into solution C throughout the entire reaction.

3.4. Synthesis of NiFe-LDH

In a typical synthesis, 0.6 M $\text{Ni}(\text{NO}_3)_2 \cdot 6\text{H}_2\text{O}$ and 0.2 M $\text{Fe}(\text{NO}_3)_3 \cdot 9\text{H}_2\text{O}$ were dissolved in 20 mL DI water. This solution was labeled as solution A. 1 M NaOH was dissolved in DI water and labeled as solution B. 2 g NaNO_3 was dissolved in 100 mL DI water, which was labeled as solution C. After heating solution C to 80 °C, solutions A and B were added dropwise while the pH of solution C was maintained at around 10. After 10 min, the product was collected by centrifugation, washed with DI water and ethanol several times, and dried in freeze dryer for 24 h. Nitrogen gas was bubbled into solution C throughout the entire reaction.

3.5. Synthesis of U-NiFeZnCoAl-LDH

The preparation of U-NiFeZnCoCr-LDH followed a modified co-precipitation method. In a typical synthesis, 0.2 M $\text{Ni}(\text{NO}_3)_2 \cdot 6\text{H}_2\text{O}$, 0.1 M $\text{Fe}(\text{NO}_3)_3 \cdot 9\text{H}_2\text{O}$, 0.2 M ZnCl_2 , 0.2 M $\text{Co}(\text{NO}_3)_2 \cdot 6\text{H}_2\text{O}$ and 0.1 M $\text{Al}(\text{NO}_3)_3 \cdot 9\text{H}_2\text{O}$ were dissolved in 20 mL DI water. This solution was labeled as solution A. 1 M NaOH was dissolved in DI water and labeled as solution B. 2 g NaNO_3 was dissolved in 77 mL DI water, then 23 mL FA was added and the mixture was stirred magnetically to form a homogeneous solution, which was labeled as solution C. After heating solution C to 80 °C, solutions A and B were added dropwise while the pH of solution C was maintained at around 10. After 10 min, the product was collected by centrifugation, washed with DI water and ethanol several times, and dried in freeze dryer for 24 h. Nitrogen gas was bubbled into solution C throughout the entire reaction.

3.6. Synthesis of U-NiFeZnCoMn-LDH

The preparation of U-NiFeZnCoCr-LDH followed a modified co-precipitation method. In a typical synthesis, 0.2 M $\text{Ni}(\text{NO}_3)_2 \cdot 6\text{H}_2\text{O}$, 0.1 M $\text{Fe}(\text{NO}_3)_3 \cdot 9\text{H}_2\text{O}$, 0.2 M ZnCl_2 , 0.2 M $\text{Co}(\text{NO}_3)_2 \cdot 6\text{H}_2\text{O}$ and 0.1 M $\text{Mn}(\text{NO}_3)_2 \cdot 4\text{H}_2\text{O}$ were dissolved in 20 mL DI water. This solution was labeled as solution A. 1 M NaOH was dissolved in DI water and labeled as solution B. 2 g NaNO_3 was dissolved in 77 mL DI water, then 23 mL FA was added and the mixture was stirred magnetically to form a homogeneous solution, which was labeled as solution C. After heating solution C to 80 °C, solutions A and B were added dropwise while the pH of solution C was maintained at around 10. After 10 min, the product was collected

by centrifugation, washed with DI water and ethanol several times, and dried in freeze dryer for 24 h. Nitrogen gas was bubbled into solution C throughout the entire reaction.

3.7. Synthesis of NiFeZnCoAl-LDH

In a typical synthesis, 0.2 M Ni(NO₃)₂·6H₂O, 0.1 M Fe(NO₃)₃·9H₂O, 0.2 M ZnCl₂, 0.2 M Co(NO₃)₂·6H₂O and 0.1 M Al(NO₃)₃·9H₂O were dissolved in 20 mL DI water. This solution was labeled as solution A. 1 M NaOH was dissolved in DI water and labeled as solution B. 2 g NaNO₃ was dissolved in 100 mL DI water, which was labeled as solution C. After heating solution C to 80 °C, solutions A and B were added dropwise while the pH of solution C was maintained at around 10. After 10 min, the product was collected by centrifugation, washed with DI water and ethanol several times, and dried in freeze dryer for 24 h. Nitrogen gas was bubbled into solution C throughout the entire reaction.

3.8. Synthesis of NiFeZnCoMn-LDH

In a typical synthesis, 0.2 M Ni(NO₃)₂·6H₂O, 0.1 M Fe(NO₃)₃·9H₂O, 0.2 M ZnCl₂, 0.2 M Co(NO₃)₂·6H₂O and 0.1 M Mn(NO₃)₂·4H₂O were dissolved in 20 mL DI water. This solution was labeled as solution A. 1 M NaOH was dissolved in DI water and labeled as solution B. 2 g NaNO₃ was dissolved in 100 mL DI water, which was labeled as solution C. After heating solution C to 80 °C, solutions A and B were added dropwise while the pH of solution C was maintained at around 10. After 10 min, the product was collected by centrifugation, washed with DI water and ethanol several times, and dried in freeze dryer for 24 h. Nitrogen gas was bubbled into solution C throughout the entire reaction.

3.9. Materials Characterization

The size and morphology of the samples were characterized using a field-emission scanning electron microscope (SEM, Zeiss Supra 55, Hamburg, Germany) operated at 20 kV. An EDS equipped on the SEM was employed to record the element distribution. High-resolution TEM (HRTEM) images were acquired with JEOL JEM-2100 operated at 200 kV. Atomic force microscope (AFM, Bruker Dimension Icon, Bremen, Germany) for thickness of nanosheets. The valence composition of the samples was performed by X-ray photoelectron spectroscopy (XPS, Axis Supra, Tokyo, Japan) with the non-monochromatic Al K α X-ray as the X-ray source. The crystal structures of the samples were measured by a powder X-ray diffractometer (Bruker D8A25, Bremen, Germany) using Cu-K α radiation. Infrared Spectroscopy (IR) was performed by Thermo Fisher Nicolet 6700, Waltham, MA, USA. The metal elements content of samples was determined by inductively coupled plasma mass spectroscopy (ICP-MS, Thermo Fisher ICAP-6300, Waltham, MA, USA).

3.10. Electrochemical Measurements

The as-prepared catalysts were prepared by ultrasonically mixing 5 mg of the catalysts powder, 1 mL ethanol and 10 μ L 5% Nafion solution for at least 1h to form homogeneous catalyst inks. For the preparation of the catalytic electrodes, 1 mL ink was carefully dropped onto Ni foam (1 cm \times 1 cm), so the catalyst loading amount could be calculated as 5 mg cm⁻². Electrocatalytic experiments were performed on a CHI 660D electrochemical analyzer (CH Instruments, Inc., Shanghai, China) with a three-electrode cell system for OER. The catalyst ink-loaded Ni foam (1 cm \times 1 cm) was used as working electrode. A platinum electrode and a saturated calomel electrode (SCE) were used as counter and reference electrodes, respectively. All measured potentials vs. SCE were converted to a reversible hydrogen electrode (RHE) according to the Nernst equation ($E_{\text{RHE}} = E_{\text{SCE}} + 0.059 \text{ pH} + 0.244 \text{ V}$). Polarization curves were obtained using cyclic voltammetry (CV) with a scan rate of 5 mV s⁻¹. All polarization curves were corrected for Ohmic drops tested by electrochemical impedance spectroscopy (EIS). The EIS was obtained in 1 M KOH solution by applying an AC voltage of 5 mV amplitude at open circuit potential with a frequency from 100 kHz to 0.1 Hz.

3.11. ECSA Measurements

The electrochemical double-layer capacitance (C_{dl}) was calculated using CV in a potential range of 1.17–1.25 V. In this voltage range, there is no peak caused by the kinetic polarization. The scan rates were controlled at 20, 40, 60, 80 and 100 mV s^{-1} . Collect the current densities J_p and J_n during positive and negative scans when the potential reaches 1.21 V vs. RHE, and calculate the current density $(J_p - J_n)/2$. Fit this current density with the scan speed. The slope obtained is double-layer capacitance (C_{dl}). The ECSA of a catalyst sample was calculated from the double-layer capacitance according to $\text{ECSA} = C_{dl}/C_s$, where C_s is the specific capacitance of the sample.

4. Conclusions

Ultrathin high-entropy layered double hydroxides, synthesized through a simple one-step method, exhibit exceptional electrochemical activity and stability. The obtained ultrathin high-entropy layered double hydroxides material possesses a layered single-phase structure with uniform distribution of various elements, demonstrating a remarkable degree of dispersion. Leveraging its unique high-entropy structure, this novel catalytic platform for water oxidation shows low overpotential and fast kinetics. Furthermore, it demonstrates excellent performance in Ampere-level long-term stability tests. This study presents an opportunity for simple synthesis of outstanding electrocatalytic high-entropy hydroxide materials while expanding our understanding of the realm of high-entropy materials.

Supplementary Materials: The following supporting information can be downloaded at: <https://www.mdpi.com/article/10.3390/catal14030171/s1>, Figure S1. XRD patterns of NiFeZnCoCr-LDH, NiFeZnCoMn-LDH, NiFeZnCoAl-LDH, U-NiFeZnCoCr-LDH, U-NiFeZnCoMn-LDH and U-NiFeZnCoAl-LDH; Figure S2. EDS-mapping of U-NiFeZnCoCr-LDH and U-NiFeZnCoMn-LDH; Figure S3. High-resolution Zn 2p XPS; Figure S4. High-resolution Cr 2p XPS; Figure S5. (a) Polarization curves of NiFe-LDH, NiFeZnCoCr-LDH, U-NiFeZnCoCr-LDH and Ni foam. (b) The redox peaks of Ni foam; Figure S6. The polarization curves of NiFe-LDH, NiFeZnCoCr-LDH and U-NiFeZnCoCr-LDH for estimates of the C_{dl} and ECSA; Figure S7. (a) Polarization curves, (b) Tafel slope of NiFe-LDH, NiFeZnCoCr-LDH, NiFeZnCoMn-LDH, NiFeZnCoAl-LDH, U-NiFeZnCoCr-LDH, U-NiFeZnCoMn-LDH and U-NiFeZnCoAl-LDH.

Author Contributions: Conceptualization, J.J., D.Z., Y.L. and X.S.; methodology, J.J., X.D., W.X. and M.M.; validation, J.J.; investigation, J.J., W.L. and T.L.; writing—original draft preparation, J.J., W.L. and D.Z.; writing—review and editing, W.L., D.Z., Y.L. and X.S.; visualization, J.J. and W.L.; supervision, D.Z., Y.L. and X.S.; funding acquisition, D.Z., Y.L. and X.S. All authors have read and agreed to the published version of the manuscript.

Funding: This work was supported by the Science and Technology Innovation Foundation of Laoshan Laboratory (No. LSKJ202205700), the Xinjiang Uygur Autonomous Region Key R&D Projects (No. 202114958) and Shenzhen Energy Group Co., Ltd. The authors also thank the Fundamental Research Funds for the Central Universities, and the long-term subsidy mechanism from the Ministry of Finance and the Ministry of Education of China.

Data Availability Statement: The data presented in this study are available on request from the corresponding authors.

Conflicts of Interest: The authors declare no conflict of interest.

References

1. Xie, H.; Zhao, Z.; Liu, T.; Wu, Y.; Lan, C.; Jiang, W.; Zhu, L.; Wang, Y.; Yang, D.; Shao, Z. A Membrane-Based Seawater Electrolyser for Hydrogen Generation. *Nature* **2022**, *612*, 673–678. [[CrossRef](#)]
2. Ou, Y.; Twight, L.P.; Samanta, B.; Liu, L.; Biswas, S.; Fehrs, J.L.; Sagui, N.A.; Villalobos, J.; Morales-Santelices, J.; Antipin, D.; et al. Cooperative Fe Sites on Transition Metal (Oxy)Hydroxides Drive High Oxygen Evolution Activity in Base. *Nat. Commun.* **2023**, *14*, 7688. [[CrossRef](#)] [[PubMed](#)]
3. Liu, T.; Chen, Y.; Hao, Y.; Wu, J.; Wang, R.; Gu, L.; Yang, X.; Yang, Q.; Lian, C.; Liu, H.; et al. Hierarchical Anions at the Electrode-Electrolyte Interface for Synergized Neutral Water Oxidation. *Chem* **2022**, *8*, 2700–2714. [[CrossRef](#)]

4. Lee, S.; Chu, Y.-C.; Bai, L.; Chen, H.M.; Hu, X. Operando Identification of a Side-on Nickel Superoxide Intermediate and the Mechanism of Oxygen Evolution on Nickel Oxyhydroxide. *Chem Catal.* **2023**, *3*, 100475. [[CrossRef](#)]
5. Tao, H.B.; Xu, Y.; Huang, X.; Chen, J.; Pei, L.; Zhang, J.; Chen, J.G.; Liu, B. A General Method to Probe Oxygen Evolution Intermediates at Operating Conditions. *Joule* **2019**, *3*, 1498–1509. [[CrossRef](#)]
6. Chen, C.; Jin, H.; Wang, P.; Sun, X.; Jaroniec, M.; Zheng, Y.; Qiao, S.-Z. Local Reaction Environment in Electrocatalysis. *Chem. Soc. Rev.* **2024**, *53*, 2022–2055. [[CrossRef](#)] [[PubMed](#)]
7. Yang, Y.; Li, P.; Zheng, X.; Sun, W.; Dou, S.X.; Ma, T.; Pan, H. Anion-Exchange Membrane Water Electrolyzers and Fuel Cells. *Chem. Soc. Rev.* **2022**, *51*, 9620–9693. [[CrossRef](#)] [[PubMed](#)]
8. Zeng, S.-P.; Shi, H.; Dai, T.-Y.; Liu, Y.; Wen, Z.; Han, G.-F.; Wang, T.-H.; Zhang, W.; Lang, X.-Y.; Zheng, W.-T.; et al. Lamella-Heterostructured Nanoporous Bimetallic Iron-Cobalt Alloy/Oxyhydroxide and Cerium Oxynitride Electrodes as Stable Catalysts for Oxygen Evolution. *Nat. Commun.* **2023**, *14*, 1811. [[CrossRef](#)]
9. Danyang He, L.C. In-situ optimizing the valence configuration of vanadium sites in NiV-LDH nanosheet arrays for enhanced hydrogen evolution reaction. *J. Energy Chem.* **2020**, *47*, 263. [[CrossRef](#)]
10. Wang, Y.; Zhang, Y.; Liu, Z.; Xie, C.; Feng, S.; Liu, D.; Shao, M.; Wang, S. Layered Double Hydroxide Nanosheets with Multiple Vacancies Obtained by Dry Exfoliation as Highly Efficient Oxygen Evolution Electrocatalysts. *Angew. Chem. Int. Ed.* **2017**, *56*, 5867–5871. [[CrossRef](#)]
11. Chen, R.; Hung, S.-F.; Zhou, D.; Gao, J.; Yang, C.; Tao, H.; Yang, H.B.; Zhang, L.; Zhang, L.; Xiong, Q.; et al. Layered Structure Causes Bulk NiFe Layered Double Hydroxide Unstable in Alkaline Oxygen Evolution Reaction. *Adv. Mater.* **2019**, *31*, 1903909. [[CrossRef](#)]
12. You, H.; Wu, D.; Si, D.; Cao, M.; Sun, F.; Zhang, H.; Wang, H.; Liu, T.-F.; Cao, R. Monolayer NiIr-Layered Double Hydroxide as a Long-Lived Efficient Oxygen Evolution Catalyst for Seawater Splitting. *J. Am. Chem. Soc.* **2022**, *144*, 9254–9263. [[CrossRef](#)]
13. Liu, D.; Du, Y.; Li, T.; Zhang, H.; Liu, D.; Zhang, W.; Tang, H.; Hou, Y.; Li, J.; Yan, S.; et al. One-Step Synthesis of IrO_x-Decorated Ultrathin NiFe LDH Nanosheets for Efficient Oxygen Evolution Reaction. *Chem. Commun.* **2020**, *56*, 11465–11468. [[CrossRef](#)]
14. Zhang, J.; Liu, J.; Xi, L.; Yu, Y.; Chen, N.; Sun, S.; Wang, W.; Lange, K.M.; Zhang, B. Single-Atom Au/NiFe Layered Double Hydroxide Electrocatalyst: Probing the Origin of Activity for Oxygen Evolution Reaction. *J. Am. Chem. Soc.* **2018**, *140*, 3876–3879. [[CrossRef](#)]
15. Lu, Z.; Qian, L.; Tian, Y.; Li, Y.; Sun, X.; Duan, X. Ternary NiFeMn Layered Double Hydroxides as Highly-Efficient Oxygen Evolution Catalysts. *Chem. Commun.* **2016**, *52*, 908–911. [[CrossRef](#)]
16. Zhou, L.; Zhang, C.; Zhang, Y.; Li, Z.; Shao, M. Host Modification of Layered Double Hydroxide Electrocatalyst to Boost the Thermodynamic and Kinetic Activity of Oxygen Evolution Reaction. *Adv. Funct. Mater.* **2021**, *31*, 2009743. [[CrossRef](#)]
17. Sarkar, A.; Wang, Q.; Schiele, A.; Chellali, M.R.; Bhattacharya, S.S.; Wang, D.; Brezesinski, T.; Hahn, H.; Velasco, L.; Breitung, B. High-Entropy Oxides: Fundamental Aspects and Electrochemical Properties. *Adv. Mater.* **2019**, *31*, 1806236. [[CrossRef](#)] [[PubMed](#)]
18. Ma, Y.; Ma, Y.; Wang, Q.; Schweidler, S.; Botros, M.; Fu, T.; Hahn, H.; Brezesinski, T.; Breitung, B. High-Entropy Energy Materials: Challenges and New Opportunities. *Energy Environ. Sci.* **2021**, *14*, 2883–2905. [[CrossRef](#)]
19. George, E.P.; Raabe, D.; Ritchie, R.O. High-Entropy Alloys. *Nat. Rev. Mater.* **2019**, *4*, 515–534. [[CrossRef](#)]
20. Xin, Y.; Li, S.; Qian, Y.; Zhu, W.; Yuan, H.; Jiang, P.; Guo, R.; Wang, L. High-Entropy Alloys as a Platform for Catalysis: Progress, Challenges, and Opportunities. *ACS Catal.* **2020**, *10*, 11280–11306. [[CrossRef](#)]
21. Chen, Z.; Wu, J.; Chen, Z.; Yang, H.; Zou, K.; Zhao, X.; Liang, R.; Dong, X.; Menezes, P.W.; Kang, Z. Entropy Enhanced Perovskite Oxide Ceramic for Efficient Electrochemical Reduction of Oxygen to Hydrogen Peroxide. *Angew. Chem. Int. Ed.* **2022**, *61*, e202200086. [[CrossRef](#)]
22. Wang, D.; Liu, Z.; Du, S.; Zhang, Y.; Li, H.; Xiao, Z.; Chen, W.; Chen, R.; Wang, Y.; Zou, Y.; et al. Low-Temperature Synthesis of Small-Sized High-Entropy Oxides for Water Oxidation. *J. Mater. Chem. A* **2019**, *7*, 24211–24216. [[CrossRef](#)]
23. Rost, C.M.; Sacht, E.; Borman, T.; Moberg, A.; Dickey, E.C.; Hou, D.; Jones, J.L.; Curtarolo, S.; Maria, J.-P. Entropy-Stabilized Oxides. *Nat. Commun.* **2015**, *6*, 8485. [[CrossRef](#)]
24. Jin, T.; Sang, X.; Unocic, R.R.; Kinch, R.T.; Liu, X.; Hu, J.; Liu, H.; Dai, S. Mechanochemical-Assisted Synthesis of High-Entropy Metal Nitride via a Soft Urea Strategy. *Adv. Mater.* **2018**, *30*, 1707512. [[CrossRef](#)] [[PubMed](#)]
25. Sarker, P.; Harrington, T.; Toher, C.; Oses, C.; Samiee, M.; Maria, J.-P.; Brenner, D.W.; Vecchio, K.S.; Curtarolo, S. High-Entropy High-Hardness Metal Carbides Discovered by Entropy Descriptors. *Nat. Commun.* **2018**, *9*, 4980. [[CrossRef](#)]
26. Lin, Y.; Wang, H.; Peng, C.-K.; Bu, L.; Chiang, C.-L.; Tian, K.; Zhao, Y.; Zhao, J.; Lin, Y.-G.; Lee, J.-M.; et al. Co-Induced Electronic Optimization of Hierarchical NiFe LDH for Oxygen Evolution. *Small* **2020**, *16*, 2002426. [[CrossRef](#)] [[PubMed](#)]
27. Rakipov, I.T.; Petrov, A.A.; Akhmediyarov, A.A.; Khachatryan, A.A.; Varfolomeev, M.A. FTIR Spectral Study of Intermolecular Interactions of C=O Groups of Amides in Solution. *J. Mol. Liq.* **2022**, *354*, 118838. [[CrossRef](#)]
28. Magnier, L.; Cossard, G.; Martin, V.; Pascal, C.; Roche, V.; Sibert, E.; Shchedrina, I.; Bousquet, R.; Parry, V.; Chatenet, M. Fe–Ni-Based Alloys as Highly Active and Low-Cost Oxygen Evolution Reaction Catalyst in Alkaline Media. *Nat. Mater.* **2024**, 1–10. [[CrossRef](#)]
29. Chuang, T.J.; Brundle, C.R.; Rice, D.W. Interpretation of the X-Ray Photoemission Spectra of Cobalt Oxides and Cobalt Oxide Surfaces. *Surf. Sci.* **1976**, *59*, 413–429. [[CrossRef](#)]

30. Lai, C.; Li, H.; Sheng, Y.; Zhou, M.; Wang, W.; Gong, M.; Wang, K.; Jiang, K. 3D Spatial Combination of CN Vacancy-Mediated NiFe-PBA with N-Doped Carbon Nanofibers Network Toward Free-Standing Bifunctional Electrode for Zn–Air Batteries. *Adv. Sci.* **2022**, *9*, 2105925. [[CrossRef](#)]
31. Huntley, D.R.; Overbury, S.H.; Zehner, D.M.; Budai, J.D.; Brower, W.E. Surface Characterization of Amorphous and Crystallized Fe₈₀B₂₀. *Appl. Surf. Sci.* **1986**, *27*, 180–198. [[CrossRef](#)]
32. Zhou, D.; Li, P.; Lin, X.; McKinley, A.; Kuang, Y.; Liu, W.; Lin, W.-F.; Sun, X.; Duan, X. Layered Double Hydroxide-Based Electrocatalysts for the Oxygen Evolution Reaction: Identification and Tailoring of Active Sites, and Superaerophobic Nanoarray Electrode Assembly. *Chem. Soc. Rev.* **2021**, *50*, 8790–8817. [[CrossRef](#)]
33. Nakaya, Y.; Hayashida, E.; Asakura, H.; Takakusagi, S.; Yasumura, S.; Shimizu, K.; Furukawa, S. High-Entropy Intermetallics Serve Ultrastable Single-Atom Pt for Propane Dehydrogenation. *J. Am. Chem. Soc.* **2022**, *144*, 15944–15953. [[CrossRef](#)]
34. Feng, C.; Wang, F.; Liu, Z.; Nakabayashi, M.; Xiao, Y.; Zeng, Q.; Fu, J.; Wu, Q.; Cui, C.; Han, Y.; et al. A Self-Healing Catalyst for Electrocatalytic and Photoelectrochemical Oxygen Evolution in Highly Alkaline Conditions. *Nat. Commun.* **2021**, *12*, 5980. [[CrossRef](#)]
35. Xie, Q.; Cai, Z.; Li, P.; Zhou, D.; Bi, Y.; Xiong, X.; Hu, E.; Li, Y.; Kuang, Y.; Sun, X. Layered Double Hydroxides with Atomic-Scale Defects for Superior Electrocatalysis. *Nano Res.* **2018**, *11*, 4524–4534. [[CrossRef](#)]
36. Wu, Y.; Yang, J.; Tu, T.; Li, W.; Zhang, P.; Zhou, Y.; Li, J.; Li, J.; Sun, S.-G. Evolution of Cationic Vacancy Defects: A Motif for Surface Restructuration of OER Precatalyst. *Angew. Chem. Int. Ed.* **2021**, *60*, 26829–26836. [[CrossRef](#)] [[PubMed](#)]
37. Peng, L.; Yang, N.; Yang, Y.; Wang, Q.; Xie, X.; Sun-Waterhouse, D.; Shang, L.; Zhang, T.; Waterhouse, G.I.N. Atomic Cation-Vacancy Engineering of NiFe-Layered Double Hydroxides for Improved Activity and Stability towards the Oxygen Evolution Reaction. *Angew. Chem. Int. Ed.* **2021**, *60*, 24612–24619. [[CrossRef](#)]
38. Ren, X.; Li, M.; Qiu, L.; Guo, X.; Tian, F.; Han, G.; Yang, W.; Yu, Y. Cationic Vacancies and Interface Engineering on Crystalline–Amorphous Gamma-Phase Ni–Co Oxyhydroxides Achieve Ultrahigh Mass/Areal/Volumetric Energy Density Flexible All-Solid-State Asymmetric Supercapacitor. *J. Mater. Chem. A* **2023**, *11*, 5754–5765. [[CrossRef](#)]
39. Wu, Y.; Zheng, J.; Zhou, X.; Tu, T.; Liu, Y.; Zhang, P.; Tan, L.; Zhao, S. Cationic Defect-Enriched Hydroxides as Anodic Catalysts for Efficient Seawater Electrolysis. *Inorg. Chem. Front.* **2023**, *10*, 2444–2456. [[CrossRef](#)]
40. Wang, T.; Guo, M.; Zhang, X.; Cao, Y.; Wu, Q.; Tu, J.; Zhang, K. Defect-Rich NiFeAl-Layered Double Hydroxide Nanosheets for Efficient Electrocatalytic Oxygen Evolution Reaction. *ACS Appl. Nano Mater.* **2023**, *6*, 6002–6010. [[CrossRef](#)]

Disclaimer/Publisher’s Note: The statements, opinions and data contained in all publications are solely those of the individual author(s) and contributor(s) and not of MDPI and/or the editor(s). MDPI and/or the editor(s) disclaim responsibility for any injury to people or property resulting from any ideas, methods, instructions or products referred to in the content.